Bombarding energy dependence of the $^{144}Sm + ^{84}Kr$ reaction

A. C. Mignerey
Department of Chemistry, University of Maryland, College Park, Maryland 20742

K. L. Wolf* and D. G. Raich†
Argonne National Laboratory, Argonne, Illinois 60439

V. E. Viola, Jr.
Department of Chemistry and Indiana University Cyclotron Facility, Indiana University, Bloomington, Indiana 47405

J. R. Birkelund, W. U. Schröder, and J. R. Huizenga
Department of Chemistry and Nuclear Structure Research Laboratory, University of Rochester, Rochester, New York 14627
(Received 28 June 1983)

Results are presented for the damped reaction $^{144}Sm + ^{84}Kr$ at laboratory energies of 470, 595, and 720 MeV, corresponding to 1.2, 1.6, and 1.9 times the Coulomb barrier energy, respectively. Correlations between angle, kinetic-energy loss, and charge of the projectile-like fragments are discussed. A probability for orbiting is observed at all bombarding energies, with fragment kinetic energies indicative of large exit-channel deformations. This study shows that energy dissipation (up to ≈ 100 MeV) and charge exchange are correlated in a manner which appears to be independent of initial relative ion velocity. The results are compared with a classical dynamical transport model.

[NUCLEAR REACTIONS $^{144}Sm(^{84}Kr,x)$, $E_{lab}=470$, 595, and 720 MeV; measured $\sigma(\theta,E,Z)$ damped reaction products for projectile-like fragments; compared with transport model calculations.]

I. INTRODUCTION

The relative influence of conservative and dissipative forces in damped heavy-ion reactions can be studied by examining the bombarding energy dependence of the product charge, energy, and angular distributions. The deflection of the reaction products away from pure Coulomb trajectories is an important feature of these reactions which is sensitive to the damping of the radial and orbital motion during the interaction. For medium-mass nuclei and kinetic energies a few MeV/nucleon above the Coulomb barrier, systematics of the damped reaction mechanism predict angular distributions focused slightly forward of the grazing angle, with a transition to orbiting or negative-angle scattering as bombarding energy increases.[1-5]

A second important feature of the damped reaction is the conversion of kinetic energy into internal excitation energy. This kinetic energy loss, E_{loss}, coupled with the product scattering angle, has been used to derive estimates of the lifetimes of the dinuclear complex.[6] The widths of the product charge distributions have been shown to increase smoothly with E_{loss} and hence interaction time, providing clues to the role of nucleon exchange in kinetic-energy dissipation.[6,7] A wide variety of theoretical models has been proposed to interpret various features of the experimental data.[1,2,8-17] However, there is still no clear consensus as to which approach gives the most complete description of all aspects of the damped reaction mechanism. The availability of experimental data for a wide variety of systems, as a function of bombarding energy, is important in elucidating the dissipative mechanisms operating in damped heavy-ion collisions.

In the present study, the $^{144}Sm + ^{84}Kr$ reaction has been investigated at laboratory bombarding energies of 470, 595, and 720 MeV, corresponding to 1.2, 1.6, and 1.9 times the entrance-channel Coulomb barrier, evaluated at the strong-absorption radius.[18] Reactions induced by ^{84}Kr projectiles are of interest for heavy-ion studies because they represent approximately the lightest projectile for which nearly the entire reaction cross section is accounted for by the damped collision mechanism. The energy dependence of the ^{84}Kr-induced reactions on a heavy target nucleus, ^{209}Bi, has been studied previously.[19-21] The present study focuses on a lighter target, ^{144}Sm, which is spherical and highly neutron deficient ($N/Z=1.32$). Similar studies of the energy dependence of Kr-induced reactions have been carried out with a ^{139}La target,[22,23] which is also spherical but is neutron rich ($N/Z=1.44$), and with ^{168}Er,[8] which is a deformed, neutron-rich ($N/Z=1.47$) nucleus. Intercomparison of these results may yield a qualitative understanding of the influence of nuclear deformations and N/Z ratios on the effectiveness of nucleon exchange as a dissipation mechanism.

The experimental results reported here include energy, charge, and angular distributions of the projectile-like

fragments, as well as correlations among these observables. The data are interpreted both in terms of a simple nucleon-exchange calculation[9,10] and the more detailed predictions of a dynamical transport model,[9,10] based on a theory emphasizing the exchange of independent nucleons between the reaction partners as the dominant source of energy loss in damped heavy-ion reactions.[24] The latter model introduces a minimum of free parameters to account for all features of the fragment distributions, the principal assumptions relating to the family of shapes characteristic of the intermediate dinuclear system and the calculation of the Coulomb interaction potential.

The experimental procedures are summarized in the next section, followed by a discussion of the results in Sec. III. In Sec. IV, the data are interpreted in terms of both macroscopic and microscopic models with the salient conclusions of these studies presented in Sec. V.

II. EXPERIMENTAL PROCEDURE

The experiment was performed at the Lawrence Berkeley Laboratory Super-HILAC. Beams of ^{84}Kr at energies of 470, 595, and 720 MeV were used to bombard isotopically pure 150-$\mu g/cm^2$ ^{144}Sm-oxide targets. Beam intensities varied from 20- to 60-charge nA on target. Three solid state ΔE-E detector telescopes were used simultaneously to measure the charge and energy of projectile-like reaction products. The ΔE transmission detectors ranged in thickness from 16.3 to 20 μm. These were backed by 100-μm thick E detectors. Electropolished rectangular Ta apertures minimized slit scattering and defined an acceptance angle for each telescope of $\pm 0.4°$ in the reaction plane and $\pm 0.8°$ out of plane. The telescopes were protected from delta electrons by 132-$\mu g/cm^2$ Ni foils placed over the apertures. In addition, rare-earth alloy magnets placed on each side of the apertures were used to deflect the electrons away from the detectors.

Two monitor detectors at fixed angles out of the reaction plane, one on each side of the beam direction, provided a check of the beam stability by the relative intensities of their elastic peaks. Dead time correction was provided by a pulser which was triggered by a differential discriminator which was gated by elastic events in the monitor detectors. The pulser signal was then added to all electronic parameters simultaneously. This also served as a monitor of the electronic gains throughout the running period.

The measured laboratory angles were chosen to obtain complete angular distributions of the projectile-like products at intervals of 1°—2°. The angular range extended to approximately 20° back of the center-of-mass quarter-point angle. This corresponded to a range in laboratory angles of 8° to 40° at 720 MeV, 8° to 45° at 595 MeV, and 14° to 56° at 470 MeV.

The solid-state detectors were individually calibrated for energy using alpha sources and ^{252}Cf fission fragments. The resulting energy resolution of the elastically scattered ^{84}Kr ions was typically 1.5%, with the absolute beam energy known to $\sim 2\%$. Charge identification of the products was achieved by employing a relationship between the ΔE signal in the transmission detector and the total kinetic energy of the particle. To obtain a calibration curve, aluminum degraders of varying thicknesses were placed in the beam. The experimental energy-loss curve for ^{84}Kr over an energy range of 2 to 8.5 MeV/nucleon was compared with the tables of Northcliffe and Schilling.[25] A calibration function was derived which adjusted the calculated tables to agree with the measured data. Using the assumption that the same correction function applied to neighboring charges, calibration curves for Z identification of all projectile-like fragments were obtained by correcting the energy loss curves of Northcliffe and Schilling.[25] The resulting resolution was ~ 1.5 charge units for the Kr-type fragments.

Knowing the product charge, the measured kinetic energy was then corrected for the pulse-height defect in the detectors using the procedure of Kaufman *et al.*[26] A more recent parametrization by Moulton *et al.*[27] suggests that the former procedure may underestimate the pulse-height defect of high-energy heavy ions. However, the use of either procedure requires extrapolation to ion energies considerably higher than those on which the parametrizations are based. The value used for the elastically scattered 720-MeV ^{84}Kr was ~ 5 MeV. Adding the energy loss of the products in the target and Ni foil calculated using the tables of Northcliffe and Schilling,[25] the total correction for pulse-height defect and energy loss in the target and Ni foil was typically 10—12 MeV.

The internal excitation energy of the primary reaction products is dissipated mainly through the emission of light particles. Experiments have shown that at beam energies below 10 MeV/nucleon for heavy projectiles, statistical evaporation of nucleons from the fully accelerated primary fragments dominates the light-particle spectra.[28–30] The measured energy spectra must therefore be corrected for nucleon evaporation to obtain the energy spectra of the primary fragments. Since the N/Z ratio of the target is somewhat larger than that of the projectile, these corrections were performed assuming only neutron emission. This was done in an iterative procedure in which the total kinetic energy loss in the center-of-mass system was used to calculate the average number of neutrons emitted. The recoil energy owing to the undetected neutrons was then added to the initial laboratory kinetic energy and the procedure repeated until the kinetic energy converged. Throughout the calculation the excitation energy was assumed to be divided between the fragments according to the fragment masses, using the global A/Z ratio to obtain average product masses from measured product charges.

The results presented in the following sections were converted to absolute cross sections by normalizing the forward-angle elastic scattering intensity to the Rutherford cross section. The elastic and slit-scattering contributions were subtracted from the remainder of the data using a standard spectrum obtained in a small-angle run where elastic events predominated. The elastic scattering component was separated from the quasielastic events by employing the peak shape observed at small angles, corrected for kinematic broadening. To deduce the elastic peak intensity in spectra measured near the grazing angle, the standard peak was positioned according to the calcu-

lated elastic energy and normalized to the high energy portion of the observed data. The errors quoted in determination of the grazing angle and subsequent derived quantities are primarily owing to the uncertainty in differentiating elastic from quasielastic events in the vicinity of the grazing angle.

III. RESULTS

A. Reaction cross section

Two methods have been employed to estimate the reaction cross section for the system $^{144}Sm+^{84}Kr$. The two approaches, analysis of the elastic scattering and integration of the measured product distributions, are complementary, each subject to different experimental uncertainties. An elaborate optical model analysis of elastic scattering data of the quality obtained in this work did not appear warranted or instructive. It has been shown[31] that the desired information can be accurately determined from an interpretation of the elastic-scattering angular distributions in terms of the Fresnel diffraction model.[32,33]

In the Fresnel model for heavy-ion scattering,[32] the ratio of $(d\sigma/d\Omega)_{\text{elastic}}$ to $(d\sigma/d\Omega)_{\text{Rutherford}}$ falls to 0.25 at the quarter-point angle, $\theta_{1/4}$, which can be related by

$$\theta_{1/4}=2\arctan[\eta/(l_g+\tfrac{1}{2})] \tag{3.1}$$

to a grazing angular momentum l_g. By analogy to the sharp cutoff Fresnel model, l_g is usually identified with $l_{\max}$, the maximum l value leading to a reaction. In Eq. (3.1), applicable to Coulomb trajectories, the quantity $\eta=Z_PZ_Te^2/\hbar v$ is the Sommerfeld parameter, Z_P and Z_T are the projectile and target charges, and v is the relative ion velocity. The experimental quarter-point angle can also be used to obtain an estimate of the interaction radius

$$R_{\text{int}}=(\eta/k_\infty)[1+\csc(\tfrac{1}{2}\theta_{1/4})]\ , \tag{3.2}$$

where k_∞ is the asymptotic wave number. The experimental values of $\theta_{1/4}$ and the derived quantities l_g and R_{int} are tabulated in Table I for the three bombarding energies studied. The interaction radii for the 470- and 720-MeV beam energies are in good agreement, but that obtained from the 595-MeV data is much smaller. Errors made in the subtraction of quasielastic events could lead to systematically larger $\theta_{1/4}$ and hence smaller derived interaction radii.

An estimate of the total cross section has been made using the generalized Fresnel model formulated by Frahn.[33] In this approximation

$$\sigma_R=(\pi/k_\infty^2)(l_g+\tfrac{1}{2})^{1/2}\times\left\{1+\frac{2\Delta l}{(l_g+\frac{1}{2})}+\frac{\pi^2}{3}\left[\frac{\Delta l}{(l_g+\frac{1}{2})}\right]^2\right\}. \tag{3.3}$$

The parameter Δl is an angular momentum width over which the transmission coefficient decreases smoothly from 1 to 0, the effect of which is to dampen the oscillations obtained from the simple Fresnel diffraction pattern and to adjust the slope of

$$(d\sigma/d\Omega_{\text{elastic}})/(d\sigma/d\Omega_{\text{Rutherford}})$$

versus θ at angles beyond the quarter point. The reaction cross sections derived from Eq. (3.3) and quoted in Table I were obtained using a value of $\Delta l=5$ for all energies. The error estimates correspond to an error in Δl of ±5.

An alternative method of determining the total reaction cross section is integration of the measured projectile-like product distributions. This requires that all the projectile-like reaction products be detected or that accurate estimates be made for the undetected cross section. Assuming the reaction cross section is owing to either binary damped events or fusion fission, the total angular distributions shown in Fig. 1 for $20\leq Z\leq49$ have been angle integrated and the resultant cross section compared with that obtained by integration of the E_{loss} spectra in Fig. 2. Since $Z=49$ is half the charge of the combined target-projectile system, the fusion-fission component is included in the distribution. Products with $Z<20$ have been omitted, but charge distributions indicate that there is very little cross section in this region.

The major uncertainty in the integration of angular distributions arises from the extrapolation of the data to unmeasured angles. In this experiment the nature of the contour plots of total kinetic energy versus $\theta_{\text{c.m.}}$, discussed in Sec. III C, has served as a guide to estimate the shapes

TABLE I. Reaction parameters for the system $^{144}Sm+^{84}Kr$.

E_{lab}	(MeV)	470	595	720
$E_{\text{c.m.}}$	(MeV)	297	376	455
$\theta_{1/4}$ (laboratory exp)	(deg)	49.2 ±0.3	34.1 ±0.3	24.5 ±0.2
$\theta_{1/4}$ (c.m. exp)	(deg)	75.4 ±0.4	53.2 ±0.4	38.5 ±0.3
μ (reduced mass)	(u)	53.05	53.05	53.05
k_∞ (wave number)	(fm^{-1})	27.45	30.88	33.97
η (Coulomb parameter)		148.6	132.1	120.0
R_{int} (Fresnel)	(fm)	14.3 ±0.1	13.8 ±0.1	14.3 ±0.1
l_g (Fresnel exp$\theta_{1/4}$)	($\hbar$)	192 ±1	264 ±2	344 ±3
σ_R (Fresnel exp$\theta_{1/4}$)	(b)	1.63±0.09	2.39±0.15	3.32±0.10
σ_R (exp)	(b)	1.45±0.15	2.64±0.20	3.3 ±0.3
$l_{\max}$ (exp)	($\hbar$)	186 ±6	283 ±8	348 ±10
R_{SA} (exp)	(fm)	14.1 ±0.2	14.4 ±0.2	14.4 ±0.2

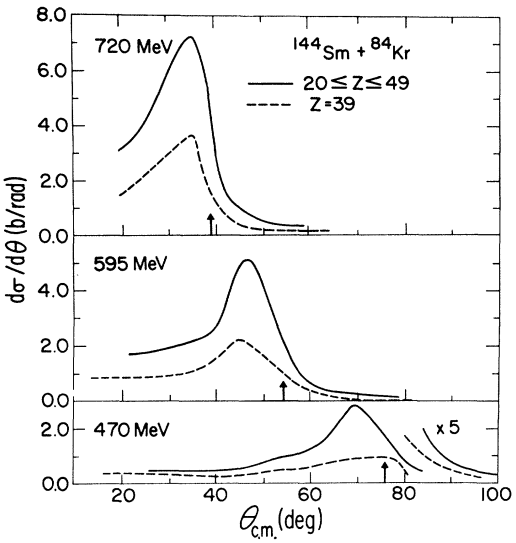

FIG. 1. Center-of-mass angular distributions of products with charge Z between 20 and 49 (solid curve) and with $Z = 39$ (dashed curve). The experimental quarter-point angles are indicated by the arrows.

of the unmeasured portions of the spectra. While the 595- and 470-MeV cases appear to have reached plateaus at forward angles, the angular distribution at 720 MeV is still decreasing at the most forward angles measured. For estimating the cross section, it was assumed that the distribution extended to zero deg in a smoothly decreasing fashion. The large errors quoted for the experimental reaction cross sections in Table I are primarily a result of the uncertainties in the forward-angle extrapolations. At each beam energy, the total cross section for angles greater than the measured region was estimated using the differential cross section measured at the largest detection angle. Since this angle was well back of the grazing angle in all cases, this procedure can be viewed to give an upper limit for a fusion-fission-like contribution. The contributions from unmeasured high-energy-loss events were estimated from Fig. 2 to be about 50 mb at each bombarding energy.

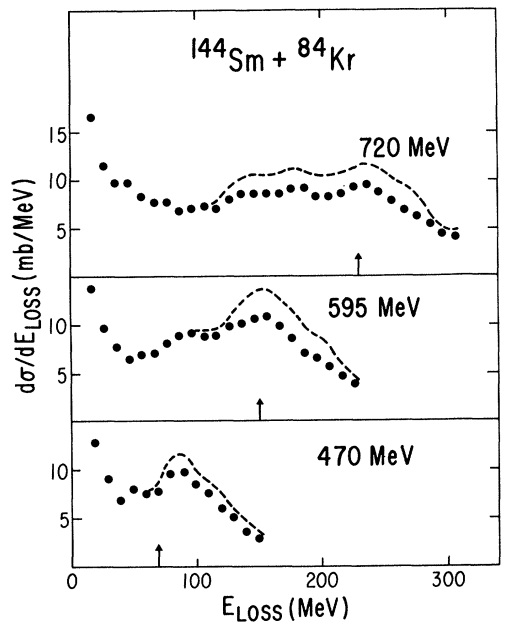

FIG. 2. Total kinetic energy spectra expressed in terms of total kinetic energy loss, E_{loss}, for products with Z between 20 and 49. The points are the result of integrating the cross section over the measured angular range presented in Fig. 1. The dashed curves include cross section estimates for angles less than 20 deg. The arrows indicate the Coulomb barrier for touching spheres at the experimental interaction radius of 14.3 fm.

Assuming a sharp cutoff model, the experimental reaction cross section can be related to a maximum angular momentum l_{max} leading to a reaction by

$$\sigma_R = (\pi/k_\infty^2)(l_{max} + \tfrac{1}{2})^2 .$$

The strong-absorption radius R_{SA} can also be estimated from

$$R_{SA} = 1/k_\infty \{\eta + [\eta^2 + l_{max}(l_{max}+1)]^{1/2}\} .$$

The reaction parameters derived from the experimental reaction cross sections are listed in Table I and are in good agreement with those obtained from the quarter-point analysis. However, the average interaction radius of 14.3 fm is considerably larger than the value of 13.6 fm which has been calculated from reaction systematics.[18] Grazing angles and maximum angular momenta calculated using this latter radius do not agree well with the reaction data quoted in Table I. The quarter-point results from ^{165}Ho and ^{154}Sm targets taken at the same time also give interaction radii which are 0.4—0.6 fm larger than predicted. Such deviations from the average trend of the systematics are not uncommon.[2]

B. Angular distributions

The angular distributions for medium-mass systems have been predicted to peak near the grazing angle for incident projectile energies near the Coulomb barrier and evolve toward progressively more forward-peaked distributions with increasing bombarding energy.[1–5] The energy-integrated, center-of-mass angular distributions for the projectile-like fragments from the $^{144}Sm + ^{84}Kr$ system at the three energies studied here are shown in Fig. 1. The solid curves are the results obtained from integrating over product Z with $20 \leq Z \leq 49$. The data include products from quasielastic, damped, and fusion-fission processes. Owing to experimental limitations, it was not possible to obtain complete charge distributions at the most forward angles ($\theta_{c.m.} < 20°$); hence, these charge-integrated differential cross sections have been omitted. The grazing angles, determined from the elastic-scattering data by the quarter-point method, are indicated as arrows in each case. All distributions are peaked slightly forward of their respective grazing angles, with considerable yield extending forward of 20°. This latter feature is generally considered indicative of the onset of negative-angle scattering or orbiting. However, the 595- and 470-MeV data exhibit plateaus at small angles, which become more pronounced

for product Z's away from that of the projectile, as is demonstrated by the dashed curve for $Z=39$. As will be shown later, this component is correlated with events of large energy loss and accounts for an increasing fraction of the elemental cross section as the product charge becomes further removed from that of the projectile. It is important to note that very little cross section extends back of the grazing angle, thus setting a limit on the contribution from fusion-fission events, which are expected to have a constant contribution at all angles in the $d\sigma/d\theta$ plot.

C. Energy spectra

The conversion of projectile kinetic energy into internal excitation of the target-projectile system is an important feature of the damped reaction process. It is frequently expressed in terms of the total kinetic energy loss, E_{loss}, calculated as the difference between the initial center-of-mass kinetic energy, $E_{\text{c.m.}}$, and the measured total kinetic energy (TKE) corrected for neutron emission (see Sec. II). Figure 2 shows the energy loss spectra $d\sigma/dE_{\text{loss}}$ for the three bombarding energies studied. The dots result from integration over the angular regions displayed in Fig. 1, while the dashed curves reflect the addition of estimated contributions from 0° to the minimum angle measured. The quasielastic events at low energy losses are clearly separated from the broad distribution of damped events. As the bombarding energy decreases, an increasing fraction of the events has kinetic energies below the entrance channel Coulomb barrier evaluated at the experimental strong-absorption radius, R_{SA} (see Table I), indicated by the arrows in Fig. 2. This suggests highly deformed geometries in the exit channel.

Additional insights into the dynamics of the reaction are obtained when the contours of constant cross section $d^2\sigma/d\theta dE$ are plotted as a function of the total kinetic energy of the system (TKE) and the center-of-mass scattering angle $\theta_{\text{c.m.}}$ (Wilczyński plot). Such contour plots for 470-, 595-, and 720-MeV ^{84}Kr are shown in Figs. 3–6. Figure 3 includes data from product charges $20 \leq Z \leq 49$, while in Figs. 4–6 the product charge has been integrated over three Z units, as indicated. The quasielastic and partially damped events are concentrated just forward of the grazing angle and correspond to products near the projectile charge of $Z=36$. In the 595- and 720-MeV cases, the cross section ridge moves continuously forward in angle with decreasing TKE (increasing E_{loss}). This behavior could be indicative of nuclear orbiting. A deflection function with nonorbiting characteristics consistent with these data should produce a rainbow at $|\theta_{\text{c.m.}}| < 10°$–$20°$.

Systematics predict that, as the bombarding energy decreases, the cross section contours become more focused in angle.[1–5] Thus, at 470 MeV a strongly focused angular distribution is expected. This is observed, however, only for the partially damped component. The fully relaxed events are distributed over a broad angular range forward of the grazing angle, quite in contrast to heavier systems,[34] where the cross section ridge extends to larger angles. This plateau persists for all product Z's and is even apparent at 720 MeV for products farthest removed in Z from the projectile. Fusion-fission and fission-like processes can be ruled out as dominant mechanisms on the basis of the low cross sections observed for these processes at backward angles.

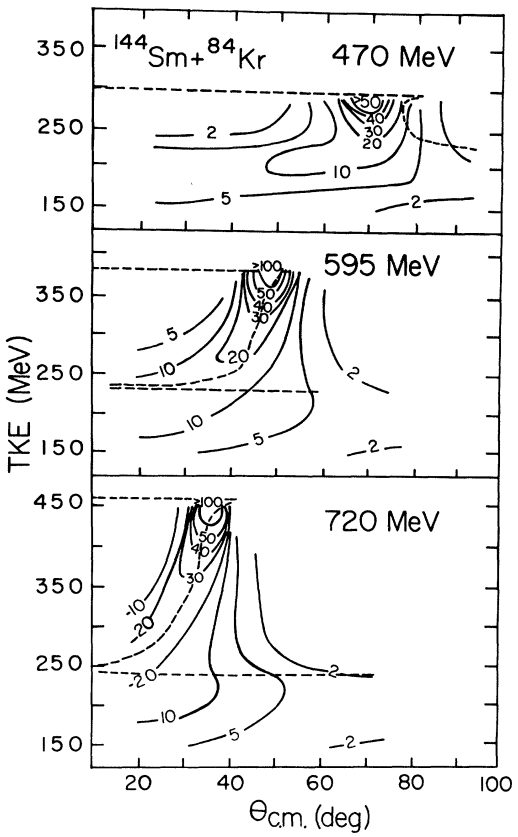

FIG. 3. Contours of constant cross section $d^2\sigma/d\theta dE$ in mb/rad MeV for products with Z between 20 and 49. The dashed curves are the results of the microscopic transport-model calculations described in Sec. IV C.

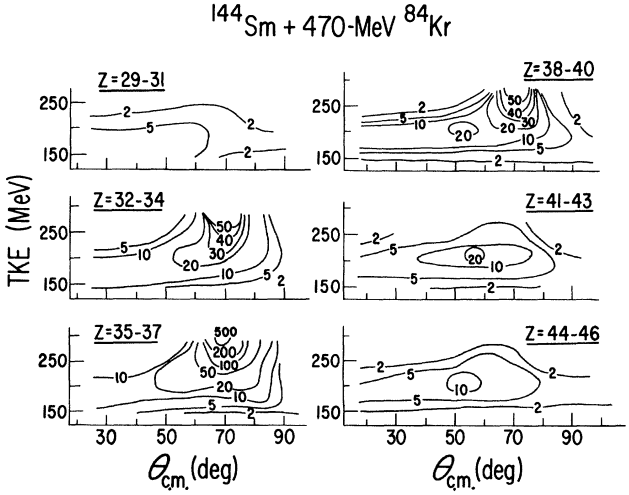

FIG. 4. Contours of constant cross section $d^2\sigma/d\theta dE$ in units of 0.1 mb/rad MeV, for the 470-MeV bombarding energy. The data are summed over three Z units, as indicated.

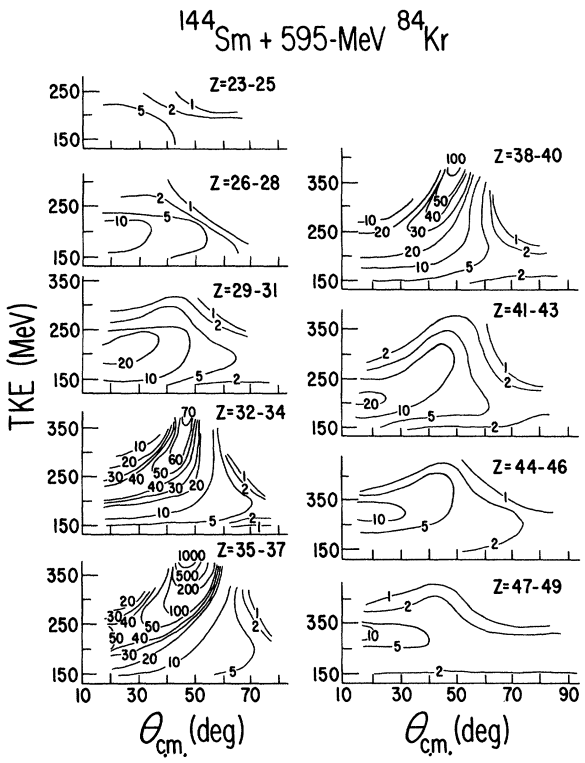

FIG. 5. Same as shown in Fig. 4 but for the 595-MeV bombarding energy.

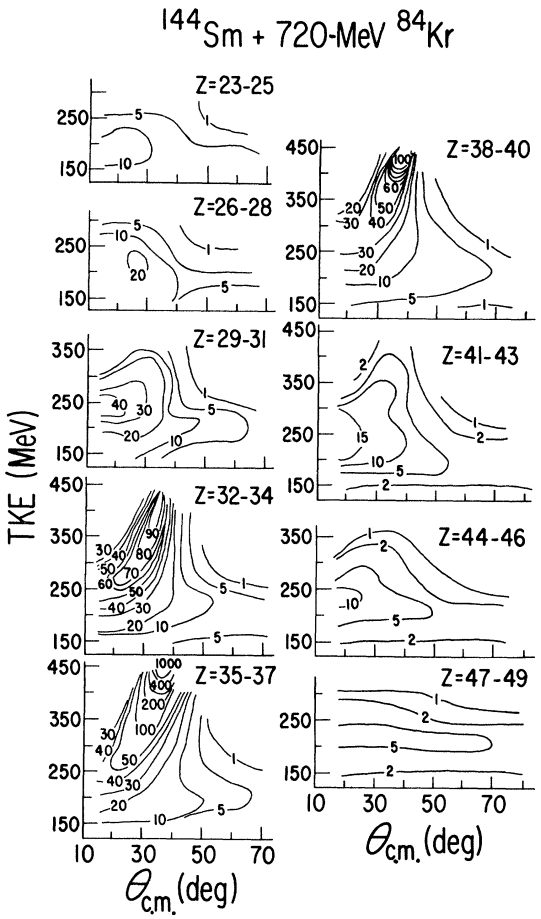

FIG. 6. Same as shown in Fig. 4 but for the 720-MeV bombarding energy.

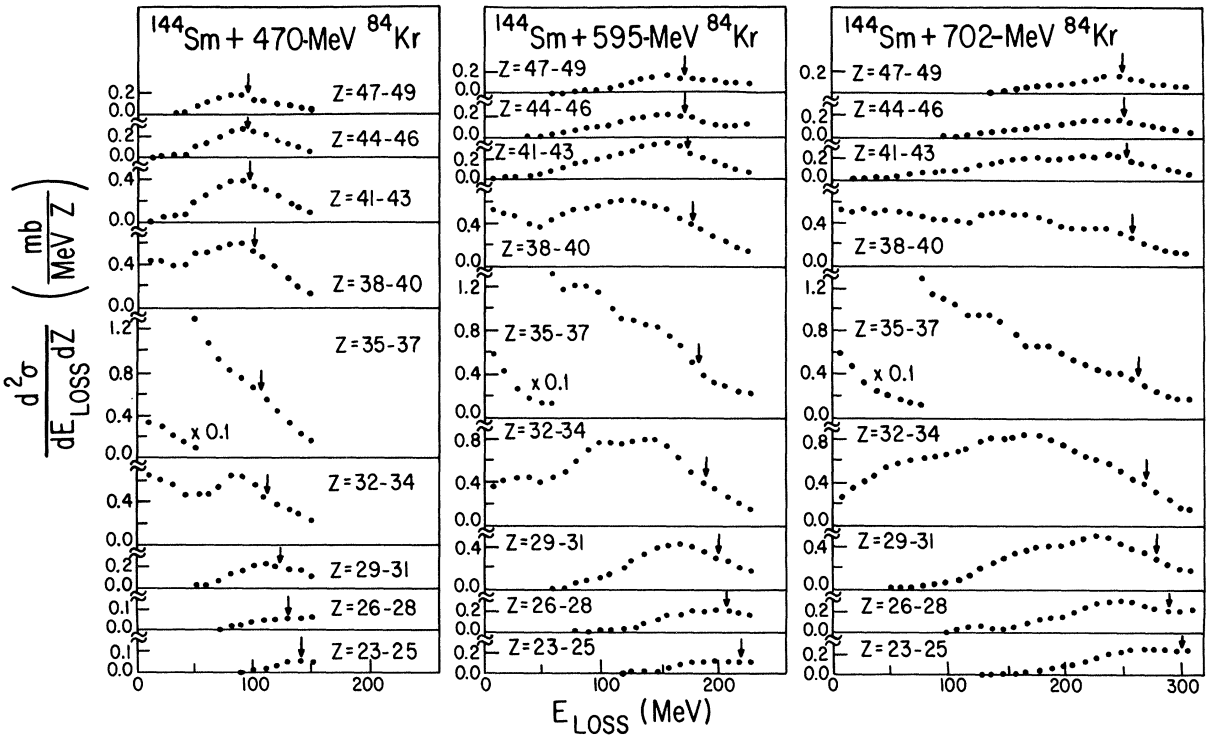

FIG. 7. Total kinetic energy loss spectra, averaged over three Z units and integrated over all measured angles. The arrows indicate Coulomb barriers for deformed fragments with the average charge of each spectrum.

The energy loss spectra corresponding to the contour plots in Figs. 4—6 are shown in Fig. 7. Except for the quasielastic energies associated with charges near the projectile, the energy loss curves are approximately Gaussian in shape. In general, the centroids move to higher energy losses with increasing distance of the fragment Z from the projectile. The arrows indicate exit-channel Coulomb energies for highly deformed elliptical fragments, calculated according to Brack *et al.*[35] for fragments with a ratio of minor to major semiaxes a/b of 0.65. The absolute cross sections for large values of E_{loss} vary little as a function of Z, suggesting broad charge distributions at all three bombarding energies. A more complete discussion of the charge distributions as a function of E_{loss} is found in the following subsection.

D. Charge distributions

The evolution of the charge distributions of the projectile-like fragments with total kinetic energy is illustrated in the contour plots of constant cross section $d^2\sigma/dE\,dZ$ as a function of TKE and Z shown in Fig. 8. For all incident beam energies, the maximum of the Z ridge remains close to that of the beam ($Z=36$), while the widths of the charge distributions increase smoothly with decreasing TKE. At low TKE a slight skewing of the cross section to Z values greater than 36 is observed for the 470-MeV beam energy, while a drift to $Z<36$ is observed for the 720-MeV beam energy. However, even at 720 MeV, a high Z asymmetry in the distribution is apparent.

There has been a great deal of discussion concerning the most valid parameter for characterizing charge distributions from reaction data. Three parameters which have been proposed are the following: (1) constant TKE,[7] (2) total kinetic energy above the Coulomb barrier[8] (TKE*), and (3) constant angular momentum.[36] In this section

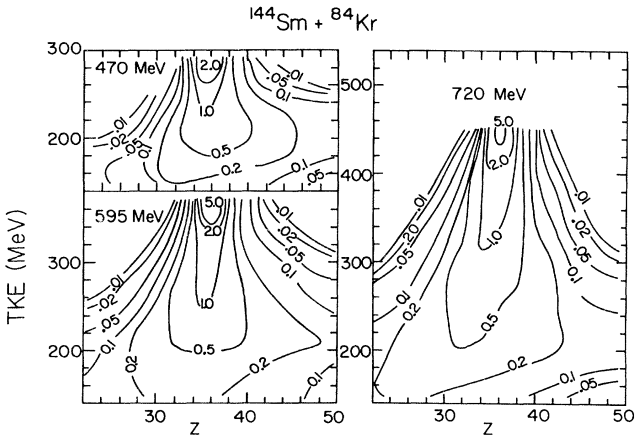

FIG. 8. Contours of constant cross section in the TKE-Z plane $d^2\sigma/dE\,dZ$ in mb/MeV-Z, integrated over the measured angular range.

constant TKE and Coulomb barrier parametrizations will be discussed and the results compared. A discussion of angular momentum effects is deferred to Sec. IV A.

For a dissipative process, energy loss increases with time. Defining charge distributions in terms of TKE (and hence E_{loss}) therefore implies a relationship to the interaction time. Cuts in the Z-TKE plane at constant TKE, corresponding to a constant reaction Q value, are model independent, although arguments have been made that TKE alone may not be the relevant parameter.[8] Representative charge distributions obtained by the TKE method are shown in Fig. 9 for data averaged over 10-MeV wide TKE bins. The curves have been labeled by their corresponding mean value of E_{loss} and only every fourth bin has been shown for clarity (every second bin for the 470-MeV data). The distributions obtained for low

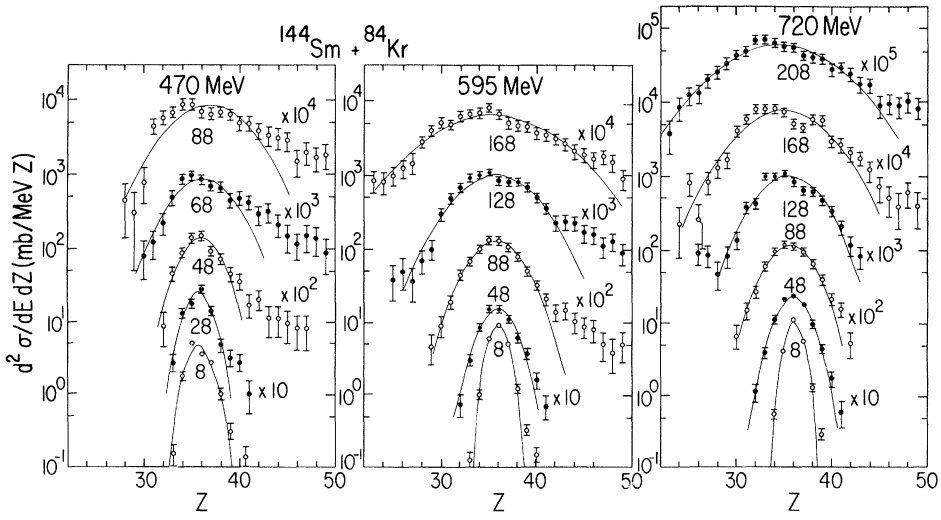

FIG. 9. Sample charge distributions obtained by averaging over 10-MeV-wide bins in TKE are shown as the points. The curves represent Gaussian fits to the data. To avoid superposition, the data and calculated fits have been multiplied by the factors indicated to the right of the data. The energy assigned to each bin is the total kinetic energy loss of the central energy of the bin.

E_{loss} are approximately Gaussian, centered near the projectile charge of $Z=36$. As energy loss increases, a high-Z tail becomes increasingly important. In reference to the contour plots of Figs. 3—6, these events are distinguished from those near the projectile Z by broad angular distributions extending forward to $\theta_{c.m.} < 20°$.

The widths of the charge distributions were derived from Gaussian fits to the data. The error minimization criteria for obtaining the best fits were applied within the limits of ± 2 standard deviations of the mean. This procedure emphasized the central portion of the data and decreased the effects of asymmetric high-Z tails. The resultant Gaussian fits to the data are shown in Fig. 9 by the solid curves. The asymmetric, high-Z component was very important in the 470-MeV data, making Gaussian fits difficult at $E_{loss} \geq 60$ MeV.

An alternative parametrization used to obtain charge distributions requires defining a total kinetic energy above the Coulomb barrier, TKE*, for each possible two-body breakup of the composite system.[8] However, there seems to be no basic physical justification for such a distinctive role of the Coulomb energy as compared to other collective energies. In addition, this procedure introduces an ambiguity in the calculation of the Coulomb barrier. As demonstrated by the energy spectra shown in Figs. 2 and 7, the kinetic energies of the fully damped products correspond to exit-channel Coulomb barriers of highly deformed fragments. These events are characterized by a broad range of products Z's, extending well into the region of symmetric ($Z_{sym}=49$) charge fragmentation. In contrast, reactions associated with small values of E_{loss} give narrow charge distributions centered near the projectile charge. In these reactions large deformations presumably do not have time to develop and spherical Coulomb barriers are probably more appropriate.

The Coulomb barriers calculated as a function of Z are plotted in Fig. 10 for both spherical[18] and deformed fragments.[35] The deformed barriers were calculated as described in Sec. III C for $a/b=0.65$. An experimental average TKE for fully relaxed products has been estimated by the average TKE of products measured at angles greater than the grazing angle. These are shown by the open circles. They fall between the spherical and deformed calculations and exhibit a relatively weak Z dependence.

The charge distributions obtained by averaging the data over 10-MeV-wide bins in TKE above the spherical Coulomb barrier, TKE*, are shown in Fig. 11. Since the Coulomb barrier is a function of Z, using such a procedure results in an energy loss which is also a function of Z. The convention used to obtain an energy loss for which results can be compared to constant TKE cuts is to define an energy loss relative to the projectile charge $Z=36$. Hence,

$$E^*_{loss} = E_{c.m.} - [\text{TKE}^* + E^{spherical}_{Coul}(Z=36)] , \quad (3.4)$$

where $E_{c.m.}$ is the elastic TKE. At small values of E^*_{loss} the charge distributions deviate little from those obtained binning by constant TKE. At higher values of E^*_{loss} the yield of charges greater than 36 is reduced and the yield of charges below 36 is enhanced relative to the constant TKE cuts, thus giving a more Gaussian shape to the resultant charge distributions. These effects are most prominent for final energies near the Coulomb barrier. A similar result is obtained for kinetic energy cuts relative to the Coulomb barrier for deformed fragments, since the curvatures of the two barriers with respect to Z are not drastically different (Fig. 10).

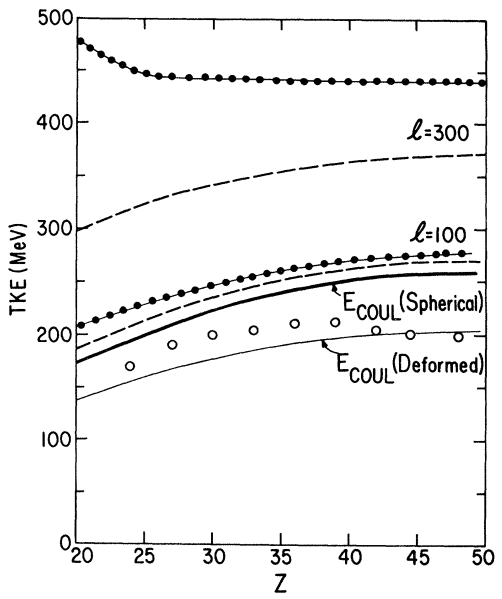

FIG. 10. The TKE calculated as a function of charge Z. Assuming the limit of infinite radial friction, Eq. (4.5) has been used for two values of initial angular momentum, $l=100$ and 300. The dotted curves correspond to the nonsticking limit and the dashed curves to the sticking limit. Both have been calculated assuming spheres in the entrance and exit channels. The thick and thin solid curves represent the Coulomb barriers for spherical and deformed fragments, respectively. The deformed case was calculated using $a/b=0.65$. The open circles have been derived from the data in Fig. 6 as the mean TKE of the cross section ridge which remains back of the grazing angle.

The variances of the charge distributions obtained from the Gaussian fits to the data shown in Figs. 9 and 11 are plotted in Fig. 12 for the three bombarding energies. The results have been corrected for the experimental charge resolution, which typically required a subtraction of 0.4—0.7 from the measured variances, depending on bombarding energy. Below 100 MeV, the two methods of energy cuts yield variances which are indistinguishable. At large energy losses the Coulomb cuts (filled symbols) give distributions slightly broader than those obtained from the constant TKE cuts (open symbols). These results are consistent with previously studied systems.[7,37,38] It is interesting to note that, while the distributions become very broad near the respective Coulomb barriers, widths for energy losses that are small in relation to the available energy above the barrier are very similar, varying little with bombarding energy. This feature will be further addressed in terms of the theoretical models discussed in Sec. IV.

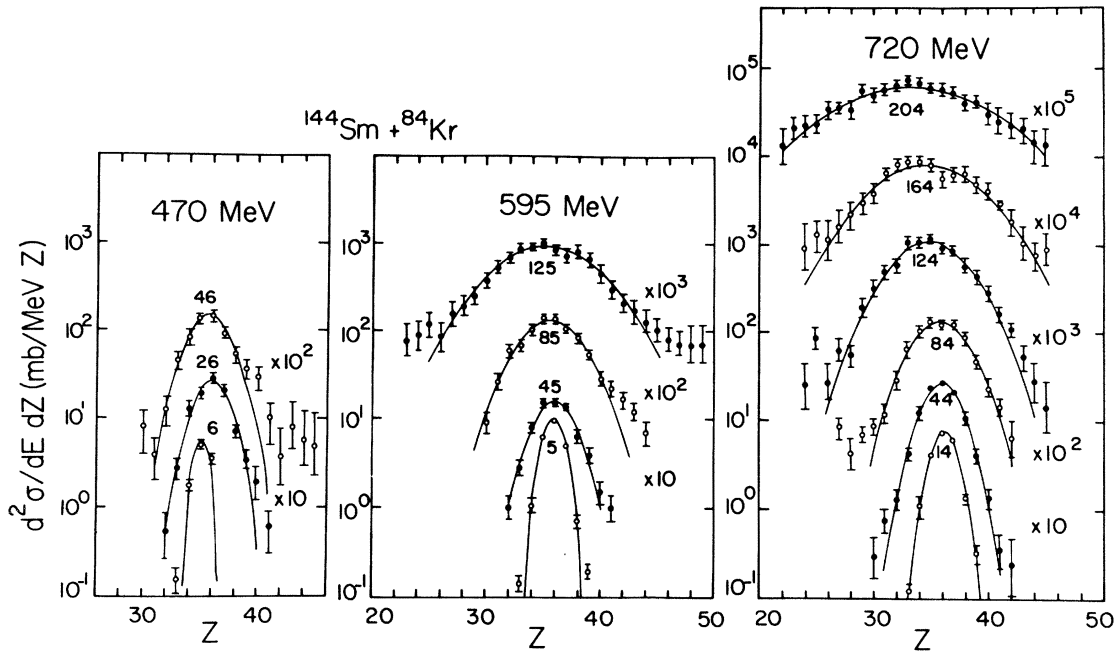

FIG. 11. Angle-integrated charge distributions obtained from averaging over 10-MeV-wide bins in TKE above the spherical Coulomb barrier are shown as the points. The curves represent Gaussian fits to the data. As in Fig. 9, points and calculated fits have been multiplied by the factors indicated. The $E^*_{\rm loss}$ assigned to each curve is based on the center of the corresponding energy bin and is calculated according to Eq. (3.4).

IV. DISCUSSION

A. Phenomenological macroscopic interpretation of data

An estimate of the angular momentum associated with a given damped reaction is central to an understanding of the dynamical evolution of the resulting dinuclear complex. Gamma-ray multiplicity studies[39–41] have shown that the angular momenta associated with processes of low $E_{\rm loss}$ are consistent with the nonsticking limit for the moment of inertia, $I_{\rm NS}$, with the initial and final angular momenta, l_i and l_f, being equal. As the interaction proceeds and kinetic energy is damped into internal excitation, the sticking limit, characterized by a final angular momentum l_f given by

$$l_f = l_i I_{\rm NS}(Z)/I_{\rm S}(Z) , \tag{4.1}$$

is approached. The moment of inertia $I_{\rm S}(Z)$ corresponds to the two reacting nuclei rotating as one rigid body. The quantities $I_{\rm NS}$ and $I_{\rm S}$ for touching spherical nuclei in the entrance and exit channels are defined by

$$I_{\rm NS}(Z) = \mu_Z r_Z^2 , \tag{4.2}$$

$$I_{\rm S}(Z) = I_{\rm NS}(Z) + 0.4(m_Z R_Z^2 + m_{Z'} R_{Z'}^2) , \tag{4.3}$$

where μ_Z and r_Z are the reduced mass and radial distance between the fragment centers, respectively. The quantities m_Z, $m_{Z'}$, R_Z, and $R_{Z'}$ are the atomic masses and radii of the individual fragments such that $Z+Z'$ equals the total charge of the composite system.

It remains to determine the angular momenta, l_i and l_f, from experimentally measured quantities. In this work the sharp cutoff approximation has been made[6,42] and applied to both TKE and $\theta_{\rm c.m.}$ variables. Referring to the contour plots of constant cross section as a function of TKE and $\theta_{\rm c.m.}$ (Fig. 3), the forward orbiting cross-section ridge is observed to be better defined by TKE at small $E_{\rm loss}$ and by $\theta_{\rm c.m.}$ at large $E_{\rm loss}$. Equating the grazing angular momentum to the maximum TKE (or the grazing angle), the l_i values are assigned to each bin in TKE (or $\theta_{\rm c.m.}$) on the basis of the cross section in that bin. The results of such an l unfolding are shown in Figs. 13 and 14

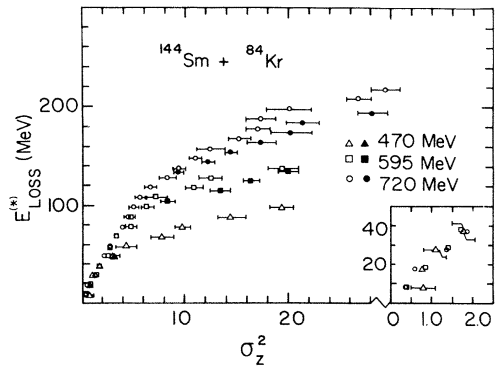

FIG. 12. The correlation between the variances of the charge distributions and the total kinetic energy loss. The open symbols are from TKE cuts ($E_{\rm loss}$) and the filled symbols are from Coulomb cuts ($E^*_{\rm loss}$). The Coulomb cuts have not been included at low $E^*_{\rm loss}$ since the points would be superimposed on the TKE cuts. Inset is an expanded plot of the variances for the initial energy losses.

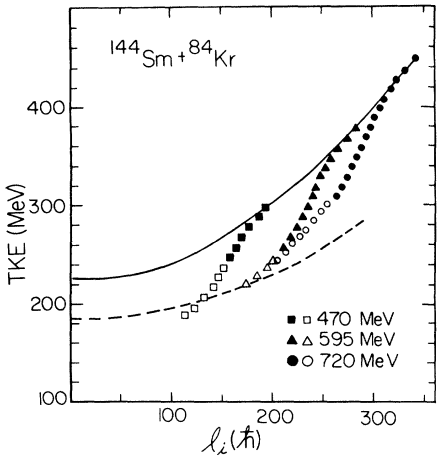

FIG. 13. The initial angular momenta derived from the sharp cutoff model are shown by the symbols. The filled symbols employed TKE cuts and the open symbols $\theta_{c.m.}$ cuts. The solid curve is the TKE calculated for spherical fragments using Eq. (4.4) and assuming a charge of $Z=36$. The dashed curve is the same calculation as applied to deformed fragments in the exit channel.

for the three bombarding energies. The solid points correspond to TKE cuts and the open points to $\theta_{c.m.}$ cuts. There is a smooth transition between the two methods, allowing utilization of the forward plateau of cross section observed in the 595- and 470-MeV cases, where the average TKE associated with a given $\theta_{c.m.}$ changes little with decreasing $\theta_{c.m.}$.

It is interesting to compare these results to the total kinetic energy calculated for the system assuming infinite radial friction. The TKE for a given l and Z fragment can then be expressed as the sum of the centrifugal energy $E_{rot}(Z,l)$ and the Coulomb energy $E_{Coul}(Z)$

$$\mathrm{TKE}(Z,l)=E_{Coul}(Z)+E_{rot}(Z,l)\ , \tag{4.4}$$

with

$$E_{rot}(Z,l)=\frac{\hbar^2 l_f^2(Z,l)}{I_{NS}(Z)}\ . \tag{4.5}$$

Using the Coulomb energy evaluated for spherical fragments, Fig. 10 shows the resulting TKE for $l_i=100$ and

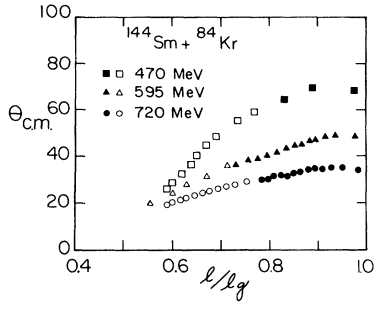

FIG. 14. The deflection angle in degrees plotted for the three incident bombarding energies in terms of relative angular momentum l/l_g. As in Fig. 13, the filled and open symbols are derived from TKE and $\theta_{c.m.}$ cuts, respectively.

300 in the sticking and nonsticking limits. The assumption of a monotonic relation between angular momentum and final TKE appears reasonable for small and intermediate energy losses, which are of interest in the present context.

The relation between TKE and initial l value derived for spherical fragments in the nonsticking limit and for a separation distance equal to the experimentally determined strong absorption radius R_{SA} is plotted as the solid line in Fig. 13. It is clear that this defines an upper limit for the TKE. The dashed line has been obtained by allowing for ellipsoidal $(a/b=0.65)$ deformations of the fragments in the exit channel.[35] These results suggest that there is a clear transition from spherical to deformed shapes with increasing E_{loss} (decreasing TKE and decreasing l_i). The transition to the sticking configuration has little effect on the deduced final TKE at low angular momenta (see Fig. 10), where small TKE values require large deformations of the dinuclear complex at breakup.

A major uncertainty in this phenomenological determination of l_i is the determination of the cross section at low TKE values and forward angles. Here it is not possible to separate the shorter-lived, positive-angle component from the longer-lived, negative-angle component. The qualitative effect of attributing all of the cross section to positive-angle scattering, as done in this work, is that derived angular momenta are too low. This effect is partly compensated for by the fact that the average TKE assigned to each reaction angle $\theta_{c.m.}$ is probably also low, thereby preserving the trend of the curves in Fig. 13. The phenomenologically derived deflection functions, shown in Fig. 14 as a function of relative angular momentum l/l_g, clearly exhibit the strong orbiting tendencies. Accounting for orbiting in the analysis would associate the larger deflections away from Coulomb trajectories with higher l/l_g values than indicated in Fig. 14. This uncertainty should be considered when comparing the experimental results to theoretical calculations.

B. Interaction time

The time scale of a reaction is of fundamental importance to the determination of the mechanisms involved. Since the interaction time τ is not a directly measurable quantity, a reaction model must be chosen for its calculation. In the present work, it is assumed that the interaction time is a function of the angle $\Delta\theta$ through which the intermediate dinuclear complex rotates during contact. This rotation angle is a function of the angular momentum in the entrance and exit channels, l_i and l_f, respectively. For a constant moment of inertia $I=I(l_i)$, the interaction time is given by

$$\tau(l_i)=\Delta\theta(l_i)I(l_i)/\hbar l_f\ , \tag{4.6}$$

with

$$\Delta\theta=\pi-\theta_C-\theta_{c.m.}\ . \tag{4.7}$$

The sum of the Coulomb deflection angles in the entrance and exit channels, θ_C, is calculated analytically.[43] The interaction times τ_{NS} and τ_S calculated using the nonsticking

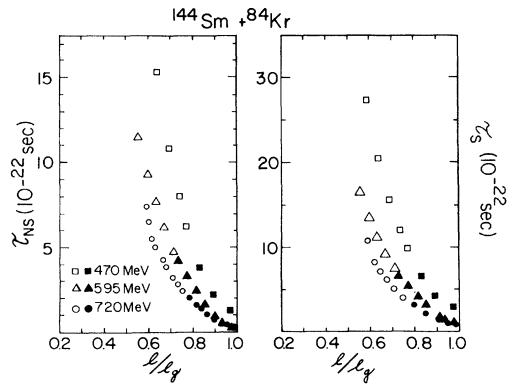

FIG. 15. The interaction times obtained from Eq. (4.6) using the nonsticking (NS) and sticking (S) limits, plotted as a function of relative angular momentum. The symbols are as described in Figs. 13 and 14.

and sticking assumptions for l_f derived in the sharp cutoff approximation are shown in Fig. 15 as a function of l/l_g. Note the change in time scale by a factor of 2 between τ_{NS} and τ_S. As in Figs. 13 and 14, the filled and open symbols represent results of binning with respect to constant TKE and $\theta_{c.m.}$, respectively. At a given l/l_g the interaction times increase sharply with decreasing bombarding energy, even near the grazing angular momenta. This result is different from that obtained for the heavier, more focused $^{209}Bi+^{136}Xe$ system,[44] where very similar interaction times were obtained for different bombarding energies. Viewing τ_S as a function of E_{loss}, Fig. 16 shows that the large plateau of cross section centered at approximately constant E_{loss} is responsible for the longest interaction times observed.

Of particular interest are the relative time scales of mass exchange and energy relaxation processes. In the application of the Fokker-Planck equation to nuclear dynamics,[45] the relationship

$$\sigma_Z^2 = 2D_Z\tau \tag{4.8}$$

is obtained in the approximation of constant transport coefficients. Adopting this simplified relation, the coefficient D_Z corresponds to the slope of σ_Z^2 vs τ plots, depicted in Fig. 17, which compares the NS and S cases for the

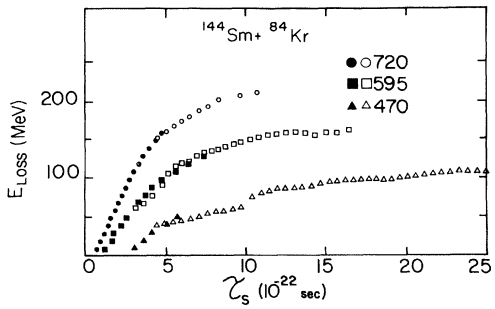

FIG. 16. The interaction times calculated in the sticking limit as a function of E_{loss} for the three incident bombarding energies. The symbols are as described in Fig. 13.

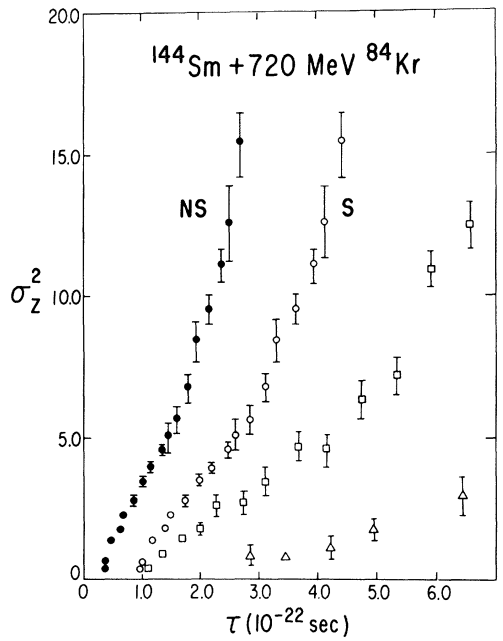

FIG. 17. The charge variances are plotted as a function of the nonsticking (filled circles) and sticking (open circles) interaction times for the 720-MeV bombarding energy. The sticking interaction times for the 595- and 470-MeV bombarding energies are shown as the squares and triangles, respectively.

720-MeV data and the S case at all three bombarding energies. Since this approximation is certainly unjustified, the absolute values of D_Z derived from Fig. 17 are not very meaningful, and more detailed treatments are available.[9,24,46–49] Qualitatively, neither the sticking nor nonsticking correlations represent a linear relationship. The change in average slope observed around $\sigma_Z^2 \sim 6$ reflects a similar feature at an energy loss of ~ 100 MeV in the data shown in Fig. 12. This may reflect a transition between nonsticking and sticking correlations. However, no conclusions can currently be drawn.

C. Microscopic interpretation of data

1. Simple nontrajectory model

In a phenomenological model described in previous works[2,6,7,42] use was made of the microscopic time scale provided by the nucleon-exchange mechanism to derive a kinetic energy dissipation rate with respect to the number of nucleons exchanged, N_{ex}.

$$-\frac{dT}{dN_{ex}} = \alpha(m/\mu)T\ , \tag{4.9}$$

where N_{ex} was related to the measured variances, σ_Z^2 or σ_A^2. In Eq. (4.9),

$$T = E_{c.m.} - E_{Coul} - E_{loss}$$

is the available relative kinetic energy above the Coulomb barrier E_{Coul}, m is the nucleon mass, and μ is the reduced

mass of the dinuclear system. The coefficient α conveys information on the character of the dissipation mechanism.

Application of a model developed by Randrup,[24] leads to the derivation[9,10,48,49] of the relation

$$T^{1/2}=T_0^{1/2}-\frac{3\pi}{16}\left[\frac{mT_F}{\mu}\right]^{1/2}\left[\frac{\sigma_N^2+\sigma_Z^2}{\sigma_Z^2}\right]\left\langle\frac{\Psi(\zeta)}{X(\zeta)}\right\rangle\sigma_Z^2 \tag{4.10}$$

between T and σ_Z^2, which is approximately valid for peripheral collisions and symmetric systems. The assumptions underlying Eq. (4.10) have been discussed previously.[48,50] The quantity T_0 refers to the entrance channel and is evaluated as $E_{\text{c.m.}}-E_{\text{Coul}}$, where E_{Coul} for the present reaction is assumed to be equal to 240 MeV, the value of the Coulomb barrier for spherical fragments evaluated at the strong-absorption radius suggested by systematics.[18] The quantity in the angular brackets represents the ratio of the dimensionless form factors[24] for the friction coefficients Ψ and the mass transport coefficients X, as a function of the surface separation ζ. A Fermi energy of $T_F=37$ MeV is used in the evaluation of Eq. (4.10). Model calculations[50] of $(\sigma_N^2+\sigma_Z^2)/\sigma_Z^2$ for the $^{144}Sm+^{84}Kr$ reaction are shown in Fig. 18 for the bombarding energies of 720, 595, and 470 MeV. For energy losses greater than about 20 MeV, this ratio is essentially constant at approximately 2.6 for all three bombarding energies. However, the parameter $\langle\Psi(\zeta)/X(\zeta)\rangle\leq 1$ is expected to vary with angular momentum or energy loss. Hence, it is difficult to estimate its value without detailed trajectory calculations. It is, therefore, regarded here as a phenomenological parameter.

The experimental values of the square root of the available energy T are plotted as a function of the Z variance, σ_Z^2, in Fig. 19 for the $^{144}Sm+^{84}Kr$ reaction at bombarding energies of 720, 595, and 470 MeV. The solid points represent the data, while the straight lines are calculated with Eq. (4.10) assuming values of $\langle\Psi(\zeta)/X(\zeta)\rangle$ of 0.58, 0.74, and 1 for the bombarding energies of 720, 595, and 470 MeV, respectively. As discussed previously for other reactions,[48,50] Eq. (4.10) gives a reasonable representation

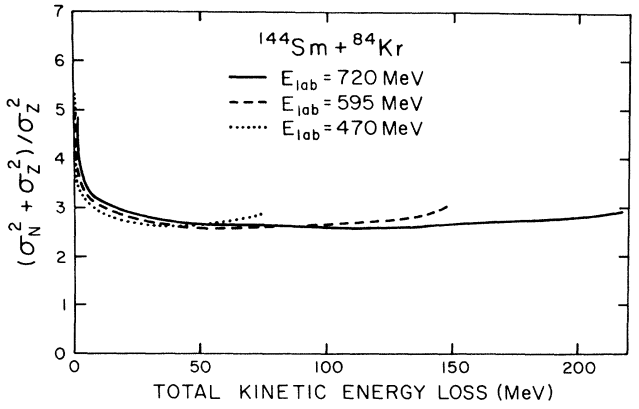

FIG. 18. Results of transport model calculations for the ratio $(\sigma_N^2+\sigma_Z^2)/\sigma_Z^2$ as a function of energy loss.

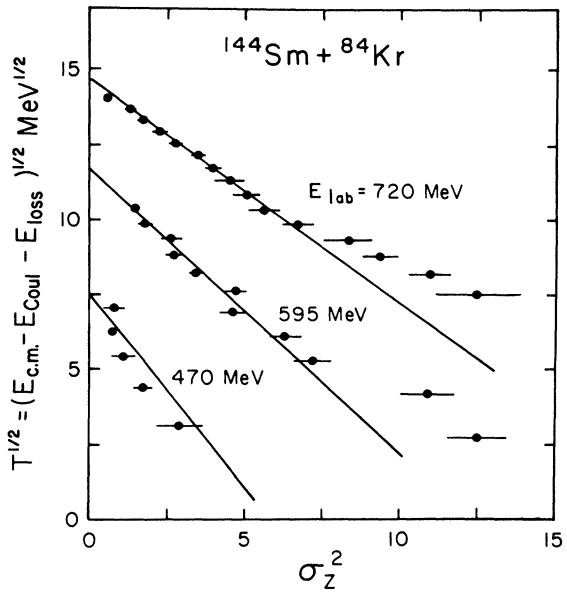

FIG. 19. Correlation of the available kinetic energy T with σ_Z^2. The solid lines represent the results of a simple model calculation [cf. Eq. (4.10)].

of the experimental data. However, the assumptions on which Eq. (4.10) is based are not adequately fulfilled, especially for the more highly dissipative events, which may not be peripheral in character. Hence, it is not surprising that the experimental points begin to deviate from the fit curves for large energy losses. On the contrary, it is quite surprising that this simple parametrization works so well for a considerable range of energy losses, as has also been noticed in simplified analyses of other heavy-ion reactions.[10,23]

2. *Dynamical calculations*

The discussion given in the preceding subsection pertains to a simplification of a reaction model proposed by Randrup,[24] in which transport phenomena occurring in damped reactions are derived solely from the fundamental microscopic mechanism of the exchange of independent nucleons between the reaction partners. Unlike the above phenomenological approach, which employs adjustable parameters and somewhat *ad hoc* assumptions, in the transport model of Randrup,[24] transport coefficients are calculated microscopically from the instantaneous conditions of the interacting system. These are specified in terms of macroscopic coordinates, such as radial separation distance, neck radius, angles of orientation, and mass and charge asymmetries of the constituents of the intermediate dinuclear system, as well as the corresponding velocities. The intrinsic system is assumed to be in thermodynamic equilibrium.

In the weak-coupling limit, on which the transport model is based, average values of macroscopic coordinates $\{\bar{q}_i,\dot{\bar{q}}_i\}$ follow classical Lagrange-Rayleigh equations of motion determined by conservative, dissipative, and inertial forces:

$$\left[\frac{d}{dt}\frac{\partial}{\partial\dot{\bar{q}}_i}-\frac{\partial}{\partial\bar{q}_i}\right]L=-\frac{\partial F}{\partial\dot{\bar{q}}_i}\ . \tag{4.11}$$

Here, $L=T-V$ is the Lagrangian, and F is the dissipation function. Kinetic-energy terms in T are evaluated for two spherical interaction partners. The potential energy V is determined from the liquid-drop model surface energy of a dumbbell-like dinuclear shape, the proximity interaction of juxtaposed surface elements outside the neck region, the liquid-drop binding energies of the two fragments, and their Coulomb interaction potential.[43] The dissipation function F describes the conversion of kinetic energy of relative motion owing to the recoil momentum and the change in the binding energies induced by nucleon exchange processes, as well as the damping of the neck motion as given by the "wall formula."[51] The time evolution of the neck radius and of average mass and charge asymmetries is assumed to be overdamped by the corresponding strong one-body friction forces, such that dynamical driving forces for these coordinates are given by the balance $\partial L/\partial\bar{q}_i=\partial F/\partial\dot{\bar{q}}_i$.

In the model, the equations of motion [cf. Eq. (4.11)] are coupled to a Fokker-Planck equation

$$\frac{d}{dt}P(N,Z,t)=\left[-\frac{\partial V_N}{\partial N}-\frac{\partial V_Z}{\partial Z}+\frac{\partial^2 D_{NN}}{\partial N^2}+\frac{\partial^2 D_{ZZ}}{\partial Z^2}\right]P(N,Z,t)\ , \tag{4.12}$$

for the time evolution of the probability distribution $P(N,Z,t)$ describing the joint probability of finding N neutrons and Z protons in one of the fragments. Drift and diffusion coefficients, V and D, respectively, are derived in Randrup's microscopic model.[24] In the calculation discussed below, the drift coefficients are expanded either to zeroth (uncorrelated case) or first (correlated case) order around the average trajectory $\{\bar{N}(t),\bar{Z}(t)\}$. This procedure yields linear coupled equations of motion for the first and second moments of P which are integrated numerically along the average system trajectory.[49] Further details of the reaction model have been reported previously.[9,48–50]

Results for the average correlation between reaction angles $\theta_{\text{c.m.}}$ and the final total kinetic energy as obtained by the model calculations are represented by dashed curves in Fig. 3 and are compared to experimental data showing the Wilczyński diagrams $d^2\sigma/d\theta\,dE$ for the reaction ^{144}Sm+^{84}Kr at $E_{\text{lab}}=720$, 595, and 470 MeV. As can be seen from the figure, the observed cross section features are reasonably well reproduced by the model trajectory for the two higher bombarding energies. Starting from the elastic energy, the cross section ridge moves forward in angle with increasing energy loss or decreasing final total kinetic energy. In agreement with the data, the calculations suggest a rate of forward deflection that increases with increasing energy loss. For large energy losses, where the initially available kinetic energy is completely damped and the fragments emerge with energies characteristic of the Coulomb repulsion of spherical or deformed nuclei, the model predicts an onset of orbiting. This behavior is consistent with a second cross section ridge observed to extend back to angles greater than the quarter-point angle and corresponding to Coulomb energies of highly deformed fragments. The exact position in energy of this "orbiting" ridge is only qualitatively reproduced by the calculations, which are unable to describe accurately the large deformations acquired in strongly damped collisions in terms of a dumbbell-like dinuclear shape. In this domain, the calculations suggest interaction times exceeding 1×10^{-21} sec, which are sufficiently[46] long for the development of deformations of the individual fragments.

In contrast to the reasonable agreement between data and calculations for energy-angle correlations obtained for the ^{144}Sm+^{84}Kr reaction at $E_{\text{lab}}=720$ and 595 MeV, the theory is clearly at variance with experiment in the case of the lowest bombarding energy of 470 MeV. Here, the cross section ridge is missed by the calculation already for very small energy losses. This is consistent with a disagreement between the experimental quarter-point angles and those predicted from reaction systematics,[18] which are approximately reproduced by the calculations. This discrepancy is greatest in the 470-MeV case (see Table I). Whereas the cross section peak for weakly damped events is located some 5° forward of the respective quarter-point angle predicted by systematics[18] in the cases of $E_{\text{lab}}=720$ MeV ($\theta_{1/4}=41.3°$) and 595 MeV ($\theta_{1/4}=54.0°$), at $E_{\text{lab}}=470$ MeV this peak is approximately 12° forward of the calculated quarter-point angle of $\theta_{1/4}=83.7°$. However, it should be noted that the experimental quarter-point angle is only 75.4°. From studies of other Kr-induced reactions,[2,22,48] one would have expected a more uniform relative forward shift of the weakly damped cross section peak, less dependent on the bombarding energy, such that the cross section pattern displayed at the top of Fig. 3 would have corresponded to a bombarding energy of 493 MeV rather than 470 MeV. However, such a large systematic error in the beam energy is unlikely.

In Fig. 20 the experimental correlations between energy loss (or negative reaction Q value) and variances σ_Z^2 of the fragment charge distributions are displayed for the ^{144}Sm+^{84}Kr reaction at the three incident energies studied. The data are the results of Gaussian fits to the experimental Z distributions shown in Fig. 12. As discussed in Sec. III, only for small energy losses are the data well described by Gaussians centered around $Z_P=36$, whereas high-Z tails develop with higher energy losses. The effect is most obvious for the lowest bombarding energy, as shown in Fig. 9, where considerable systematic uncertainty has to be ascribed to the experimental variances for energy losses greater than $\sim$50 MeV. These errors are considerably smaller for the 720- and 595-MeV data. This is verified by the small width differences between the variances derived from TKE cuts and those derived from the more symmetric Coulomb energy cuts, as shown in Fig. 12.

The transport calculations, assuming a simplified description of the fragment probability distribution $P(N,Z,t)$ in terms of a two-dimensional Gaussian, yield

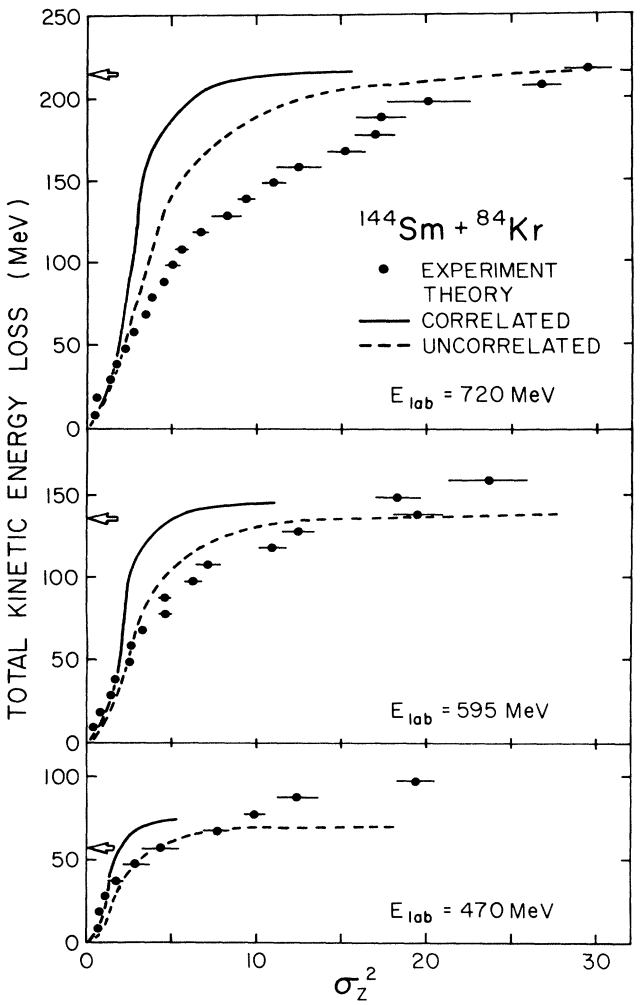

FIG. 20. Total kinetic energy loss plotted versus variance σ_Z^2 of charge distributions corresponding to cuts in TKE. The dashed and solid curves, respectively, represent model calculations neglecting or accounting for macroscopic correlations in the nucleon exchange mechanism induced by the curvature of the driving potential. Arrows indicate the initially available total kinetic energy above the entrance channel Coulomb barrier.

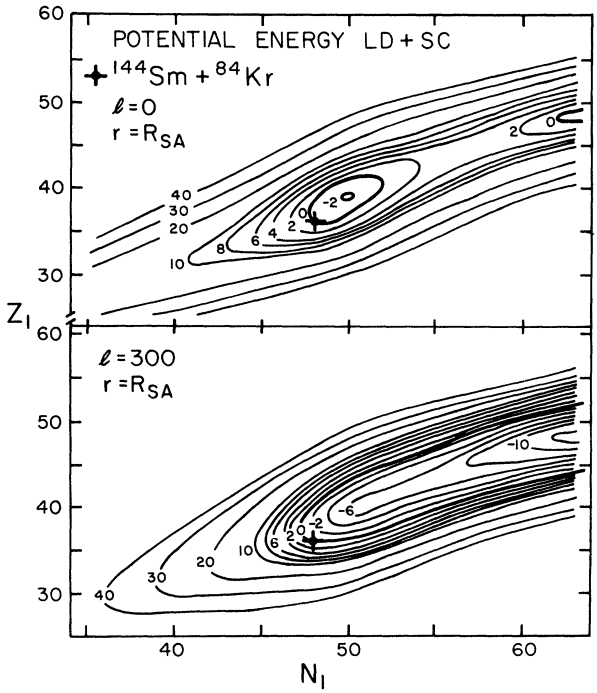

FIG. 21. Contour diagrams of the $l=0$ and 300 potential energy surfaces plotted versus proton and neutron number Z_1 and N_1, respectively, of one of the products in fragmentation of the composite system $^{144}Sm+^{84}Kr$. The energy is calculated from the shell-corrected liquid-drop model and the Coulomb potential of spherical fragments touching at the strong-absorption radius. The fragmentation $^{144}Sm+^{84}Kr$ (injection point) is indicated by a cross in each surface.

average values $\bar{Z}$ and variances σ_Z^2 as functions of the amount of energy dissipated in a collision. The results are plotted in Fig. 20 as solid and dashed curves. The solid curves are obtained using an expansion of the drift coefficients to first order in the difference of fragment proton and neutron numbers from the corresponding average values. These calculations reflect the underlying potential energy surface, shown in Fig. 21 in the form of contour diagrams plotted versus N and Z of one of the fragments for orbital angular momenta $l=0$ and 300. The potentials are derived from the liquid-drop binding energies corrected for shell effects and the nuclear, Coulomb, and centrifugal energies of two spherical fragments touching at the systematic strong-absorption separation distance R_{SA}.[18]

For small energy losses (≤ 50 MeV), comparison between the model predictions shown in Fig. 20 and the experimental data suggests an adequate description of the relation between charge and energy transport in the reaction $^{144}Sm+^{84}Kr$ at all three bombarding energies. For intermediate and large energy losses, the theoretical predictions underestimate the experimental variances to an extent that can probably not be accounted for in terms of the non-Gaussian shapes of the experimental Z distributions. Similarly, the predicted drifts of the distributions are consistent with the experimental peak positions of the charge distributions only for small energy losses. For energy losses exceeding 50—70 MeV, displacements of the distributions towards symmetry by more than 0.5 Z units are expected from the calculations. The Gaussian fits to the experimental distributions shown in Fig. 9 are clearly not in accordance with these expectations, although high-Z asymmetries of the distributions are observed to develop. It appears as if the potential energy surfaces displayed in Fig. 21, and the associated driving forces, do not properly reflect the dynamical evolution of the driving forces and their derivatives. In order to be consistent with the data, these driving forces have to be less dependent on the fragment mass and charge asymmetries than assumed in the model.

This latter point is illustrated by the dashed curves in Fig. 20, representing calculations in which the curvature of the driving potential is neglected. In this case, the driving forces cannot induce macroscopic correlations on the

nucleon exchange processes. The larger variances σ_Z^2 resulting from such a simplification are obviously in better agreement with the data than the more complete calculations in which account is taken of such correlations. However, distortions of the charge distributions owing to charged-particle emission have been neglected in the data analysis procedure. It has been shown for ^{56}Fe-induced reactions that charged particle emission can significantly distort the fragment charge distributions.[52] Charged-particle emission has been observed in the ^{197}Au+^{86}Kr reaction[53] and it is unclear what the effects might be on the more neutron deficient ^{144}Sm+^{84}Kr reaction.

V. CONCLUSION

The study of the ^{84}Kr+^{144}Sm system at bombarding energies of 720, 595, and 470 MeV yields several interesting results which are relevant to the understanding of the mechanisms through which heavy ions interact. While the partially damped events appear to follow previously observed reaction systematics, angular distributions show a plateau of cross section extending from the grazing angle forward in the 595- and 470-MeV cases. This effect can also be seen in the high-Z component of the 720-MeV data. These events are associated with long interaction times and final energies well below the entrance-channel Coulomb barrier. Similar observations in the ^{166}Er+^{84}Kr (Ref. 8) and ^{139}La+^{86}Kr (Refs. 22 and 23) reactions suggest a behavior characteristic of these intermediate-mass systems. The relative contribution of this long-lived component increases as the bombarding energy decreases, emphasizing the importance of the inclusion of deformation in present theoretical models.

Another effect which becomes increasingly important as the bombarding energy decreases is the tail of high-Z products observed near Coulomb energies. While the centroids of the projectile-like charge distributions remain constant at $Z=36$, or even drift to slightly lower Z values with increasing E_{loss}, the contribution of a high-Z component increases, producing very pronounced asymmetries in the charge distributions at large E_{loss}. This effect is reduced somewhat when charge distributions are plotted for energy bins in terms of TKE above the Coulomb barrier. However, this should not be construed as a justification for describing charge distributions in this manner. These large asymmetries may be characteristic of a separate reaction mechanism operating at kinetic energies near the Coulomb barrier. This component appears to have a pronounced drift towards symmetric splits of the composite system, and is more in keeping with the driving force of the potential energy surface (Fig. 21) than is the rest of the data. The fusion-fission-like contributions are limited by the cross sections observed at the most backward angles and are much smaller than the forward-ridge cross section observed in the angular distributions of the high-Z components. Thus, while fission-like processes[54] may contribute to the high-Z yield, they alone cannot explain the elevated cross sections observed at small angles.

The variances of the charge distributions obtained at the three bombarding energies are remarkably similar for low energy losses. In this energy range there is no significant difference between the results obtained by the TKE and Coulomb energy (TKE*) parametrizations. As the kinetic energy approaches the Coulomb barrier, the TKE* variances become larger than the TKE variances. This is largely owing to the incorporation of the high-Z component in the Gaussian fit describing the TKE* distributions.

The reaction cross sections measured in the ^{144}Sm+^{84}Kr reaction are consistently larger than those predicted from reaction systematics.[18] The experimental quarter-point angles are smaller at all three bombarding energies than the predicted values, leading to an experimental interaction radius of 14.3 fm as compared to 13.6 fm predicted from reaction systematics. The discrepancy is the greatest at the lowest bombarding energy, causing a large difference between the experimental data and model calculations.

The transport model presented appears to provide a good general description of the energy-loss process. Microscopic nucleon exchange is an effective energy-dissipation mechanism in the initial stages of the reaction. However, the neglect of fragment deformation for the strongly damped events is clearly a simplification which can be corrected through an extension of the adopted family of dinuclear shapes assumed during the interaction.

The correlations between moments of the fragment-Z distributions and the amount of kinetic energy dissipated in a collision are reproduced by the model at low energy losses for all bombarding energies. For higher energy losses, the average correlations imposed on the neutron and proton exchange processes are weaker than predicted on the basis of phenomenological liquid-drop driving forces. This problem is related to the slowness of the relaxation of the mass asymmetry degree of freedom[55] which continues to present a challenge to the current understanding of heavy-ion transport mechanisms. Further experiments where fragment masses and charges are measured simultaneously,[55] as well as information on particle emission,[56] are required to further elucidate the effect of the potential energy surface.

ACKNOWLEDGMENTS

The authors wish to thank Dr. M. Guidry and Dr. M. S. Zisman for their assistance with these experiments. In addition, we acknowledge R. Stevenson and the Super-HILAC operating crew for their cooperation in providing the ^{84}Kr beams. We are grateful to Dr. C. T. Roche and Dr. R. L. Boudrie for their participation in various aspects of this work. The excellent ^{144}Sm targets were prepared by Dr. J. Lerner. This work was performed under grants provided by the U. S. Department of Energy.

*Present address: Department of Chemistry and Cyclotron Institute, Texas A&M University, College Station, TX 77843.
†Present address: Cyclotron Corporation, Berkeley, CA 94704.

[1]A. Gobbi and W. Nörenberg, *Heavy Ion Collisions,* edited by R. Bock (North-Holland, Amsterdam, 1980), Vol. II, p. 128.
[2]W. U. Schröder and J. R. Huizenga, Annu. Rev. Nucl. Sci. 27, 465 (1977).
[3]M. Lefort and C. H. Ngô, Ann. Phys. (N.Y.) 3, 5 (1978).
[4]J. Galin, J. Phys. (Paris) 37, C5-83 (1976).
[5]L. G. Moretto and R. Schmitt, J. Phys. (Paris) 37, C5-122 (1976).
[6]W. U. Schröder, J. R. Birkelund, J. R. Huizenga, K. L. Wolf, and V. E. Viola, Jr., Phys. Rev. C 16, 623 (1977).
[7]J. R. Huizenga, J. R. Birkelund, W. U. Schröder, K. L. Wolf, and V. E. Viola, Jr., Phys. Rev. Lett. 37, 885 (1976).
[8]G. Rudolf, A. Gobbi, H. Stelzer, U. Lynen, A. Olmi, H. Sann, R. G. Stokstad, and D. Pelte, Nucl. Phys. A330, 243 (1979).
[9]W. U. Schröder, J. R. Birkelund, J. R. Huizenga, W. W. Wilcke, and J. Randrup, Phys. Rev. Lett. 44, 308 (1980).
[10]S. S. Kapoor and J. N. De, Phys. Rev. C 26, 172 (1982).
[11]K. Dietrich, Nucl. Phys. A354, 319c (1981).
[12]K. E. Rehm, H. Essel, P. Sperr, K. Hartel, P. Kienle, H. J. Korner, R. E. Segel, and W. Wagner, Nucl. Phys. A366, 477 (1981).
[13]W. Nörenberg and C. Riedel, Z. Phys. A 290, 335 (1979).
[14]M. Dakowski, A. Gobbi, and W. Nörenberg, Nucl. Phys. A378, 189 (1982).
[15]H. Feldmeier, Nukleonika 25, 171 (1980).
[16]D. H. E. Gross and K. M. Hartmann, Phys. Rev. C 24, 2526 (1981).
[17]D. H. E. Gross, R. C. Nayak, and L. Satpathy, Z. Phys. A 299, 63 (1981).
[18]W. W. Wilcke, J. R. Birkelund, H. J. Wollersheim, A. D. Hoover, J. R. Huizenga, W. U. Schröder, and L. E. Tubbs, At. Data Nucl. Data Tables 25, 389 (1980).
[19]F. Hanappe, M. Lefort, C. Ngô, J. Péter, and B. Tamain, Phys. Rev. Lett. 32, 738 (1974).
[20]K. L. Wolf, J. P. Unik, J. R. Huizenga, J. R. Birkelund, H. Freiesleben, and V. E. Viola, Jr., Phys. Rev. Lett. 33, 1105 (1974).
[21]J. R. Birkelund, H. Freiesleben, J. R. Huizenga, W. U. Schröder, W. W. Wilcke, K. L. Wolf, J. P. Unik, and V. E. Viola, Jr., Phys. Rev. C 26, 1984 (1982).
[22]R. Vandenbosch, M. P. Webb, and T. D. Thomas, Phys. Rev. Lett. 36, 459 (1976); R. Vandenbosch, M. P. Webb, P. Dyer, R. J. Puigh, R. Weisfield, T. D. Thomas, and M. S. Zisman, Phys. Rev. C 17, 1672 (1978).
[23]P. Dyer, M. P. Webb, R. J. Puigh, R. Vandenbosch, T. D. Thomas, and M. S. Zisman, Phys. Rev. C 22, 1509 (1980).
[24]J. Randrup, Nucl. Phys. A307, 317 (1978); A327, 490 (1979).
[25]L. C. Northcliffe and R. F. Schilling, Nucl. Data Tables A7, 233 (1970).
[26]S. B. Kaufman, E. P. Steinberg, B. D. Wilkins, J. Unik, A. J. Gorski, and M. J. Fluss, Nucl. Instrum. Methods 115, 47 (1974).
[27]J. B. Moulton, J. E. Stephenson, R. P. Schmidt, and G. J. Wozniak, Nucl. Instrum. Methods 157, 325 (1978).
[28]D. Hilscher, J. R. Birkelund, A. D. Hoover, W. U. Schröder, W. W. Wilcke, J. R. Huizenga, A. C. Mignerey, K. L. Wolf, H. F. Breuer, and V. E. Viola, Jr., Phys. Rev. C 20, 556 (1979).
[29]B. Tamain, R. Chechik, J. Fuchs, F. Hanappe, M. Morjean, C. Ngô, J. Péter, M. Dakowski, B, Lucas, C. Mazur, M. Ribrag, and C. Signarbieux, Nucl. Phys. A330, 253 (1979).
[30]Y. Eyal, A. Gavron, I. Tserruya, Z. Fraenkel, Y. Eisen, S. Wald, R. Bass, C. R. Gould, G. Kreyling, R. Renfordt, K. Stelzer, R. Zitzmann, A. Gobbi, U. Lynen, H. Stelzer, I. Rode, and R. Bock, Phys. Rev. C 21, 1377 (1980).
[31]J. R. Birkelund, J. R. Huizenga, H. Freiesleben, K. L. Wolf, J. P. Unik, and V. E. Viola, Jr., Phys. Rev. C 13, 133 (1976).
[32]W. E. Frahn and D. H. E. Gross, Ann. Phys. (N.Y.) 101, 520 (1976).
[33]W. E. Frahn, Nucl. Phys. A302, 267 (1978).
[34]A. Gobbi, Nucl. Phys. A354, 337c (1981).
[35]M. Brack, J. Damgaard, A. S. Jensen, H. C. Pauli, V. M. Strutinsky, and C. Y. Wong, Rev. Mod. Phys. 44, 320 (1972).
[36]J. S. Sventek and L. G. Moretto, Phys. Rev. Lett. 40, 697 (1978).
[37]W. W. Wilcke, J. R. Birkelund, A. D. Hoover, J. R. Huizenga, W. U. Schröder, V. E. Viola, Jr., K. L. Wolf, and A. C. Mignerey, Phys. Rev. C 22, 128 (1980).
[38]A. D. Hoover, J. R. Birkelund, D. Hilscher, W. U. Schröder, W. W. Wilcke, J. R. Huizenga, H. Breuer, A. C. Mignerey, V. E. Viola, Jr., and K. L. Wolf, Phys. Rev. C 25, 256 (1982).
[39]A. Olmi, H. Sann, D. Pelte, Y. Eyal, A. Gobbi, W. Kohl, U. Lynen, G. Rudolf, H. Stelzer, and R. Bock, Phys. Rev. Lett. 41, 688 (1978).
[40]L. G. Moretto and R. P. Schmidt, Phys. Rev. C 21, 204 (1980).
[41]L. G. Moretto, Nucl. Phys. A387, 331c (1982).
[42]W. U. Schröder, J. R. Birkelund, J. R. Huizenga, K. L. Wolf, and V. E. Viola, Jr., Phys. Rep. 45, 301 (1978).
[43]J. P. Bondorf, M. I. Sobel, and D. Sperber, Phys. Rev. C 15, 83 (1974).
[44]H. J. Wollersheim, W. W. Wilcke, J. R. Birkelund, and J. R. Huizenga, Phys. Rev. C 25, 338 (1982).
[45]W. Nörenberg, Phys. Lett. 52B, 289 (1974).
[46]C. Riedel, G. Wolschin, and W. Nörenberg, Z. Phys. A 290, 47 (1979).
[47]W. Nörenberg, in *Proceedings of the Nuclear Physics Workshop, International Center for Theoretical Physics, Trieste, Italy, 1981,* edited by C. H. Dasso (North-Holland, Amsterdam, 1982), p. 534.
[48]J. R. Birkelund, J. Freiesleben, J. R. Huizenga, W. U. Schröder, W. W. Wilcke, K. L. Wolf, J. P. Unik, and V. E. Viola, Jr., Phys. Rev. C 26, 1969 (1982).
[49]W. U. Schröder, J. R. Huizenga, and J. Randrup, Phys. Lett. 98B, 355 (1981).
[50]J. R. Huizenga, J. R. Birkelund, W. U. Schröder, and W. W. Wilcke, Nucl. Phys. A387, 257c (1982).
[51]W. J. Swiatecki, Lawrence Berkeley Laboratory Report LBL-8950, 1979 (unpublished).
[52]D.-K. Lock, R. Vandenbosch, and A. Lazzarini, Nucl. Phys. A384, 241 (1982).
[53]J. M. Miller, G. L. Catchen, and D. Logan, Phys. Rev. Lett. 40, 100 (1978).
[54]C. Gregoire, C. Ngô, E. Tomasi, B. Remaud, and F. Scheuter, Nucl. Phys. A387, 37c (1982).
[55]H. Breuer, A. C. Mignerey, V. E. Viola, Jr., K. L. Wolf, J. R. Birkelund, D. Hilscher, J. R. Huizenga, W. U. Schröder, and W. W. Wilcke, Phys. Rev. C 28, 1080 (1983).
[56]W. W. Wilcke, J. P. Kosky, J. R. Birkelund, M. A. Butler, A. D. Dougan, J. R. Huizenga, W. U. Schröder, and H. J. Wollersheim, Phys. Rev. Lett. 51, 99 (1983).